Application of PML Absorbing Boundary Conditions to the Benchmark Problems of Computational Aeroacoustics

Fang Q. Hu and Joe L. Manthey

Department of Mathematics and Statistics, Old Dominion University

Norfolk, VA 23529

ABSTRACT

Accurate numerical non-reflecting boundary condition is important in all the proposed benchmark problems of the Second Workshop. Recently, a new absorbing boundary condition has been developed using Perfectly Matched Layer (PML) equations for the Euler equations. In this approach, a region with a width of a few grid points is introduced adjacent to the non-reflecting boundaries. In the added region, Perfectly Matched Layer equations are constructed and applied so that the out-going waves are absorbed inside the layer with little reflection to the interior domain. It will be demonstrated in the present paper that the proposed absorbing boundary condition is quite general and versatile, applicable to radiation boundaries as well as inflow and outflow boundaries. It is also easy to implement. The emphasis of the paper will be on the application of the PML absorbing boundary condition to problems in Categories 1, 2, and 3. In Category 1, solutions of problems 1 and 2 are presented. Both problems are solved using a multi-domain polar grid system. Perfectly Matched Layer equations for a circular boundary are constructed and their effectiveness assessed. In Category 2, solutions of problem 2 are presented. Here, in addition to the radiation boundary conditions at the far field in the axisymmetric coordinate system, the inflow boundary condition at duct inlet is also dealt with using the proposed Perfectly Match Layer equations. At the inlet, a PML domain is introduced in which the incident duct mode is simulated while the waves reflected from the open end of the duct are absorbed at the same time. In Category 3, solutions of all three problems are presented. Again, the PML absorbing boundary condition is used at the inflow boundary so that the incoming vorticity wave is simulated while the outgoing acoustic waves are absorbed with very little numerical reflection. All the problems are solved using central difference schemes for spatial discretizations and the optimized Low-Dissipation and Low-Dispersion Runge-Kutta scheme for the time integration. Issues of numerical accuracy and efficiency are also addressed.

1. INTRODUCTION

Recently, a new absorbing boundary condition has been developed using Perfectly Matched Layer (PML) equations for the Euler equations^{1,2,3}. In this approach, a region with a width of a few grid points is introduced adjacent to the non-reflecting boundaries. In the added region, Perfectly

Matched Layer equations are constructed and applied so that the out-going waves are absorbed inside the layer with little reflection to the interior domain. The emphasis of the paper will be on the application PML technique to the Benchmark Problems of the workshop, as accurate numerical non-reflecting boundary condition is important in all the proposed benchmark problems. It will be demonstrated that the proposed absorbing boundary condition is quite general and versatile, applicable to radiation boundaries as well as inflow and outflow boundaries.

We present results of problems in categories 1, 2 and 3 are presented in sections 2, 3 and 4 respectively. Section 5 contains the conclusions.

2. CATEGORY 1 — PROBLEMS 1 AND 2

In Problems 1 and 2, scattering of acoustic waves by a circular cylinder is to be computed directly from the time-dependent Euler equations. To simplify the implementation of boundary conditions on the surface of the cylinder, a polar coordinate system will be used. In polar coordinates (r, θ) , the linearized Euler equations are

$$\frac{\partial u}{\partial t} + \frac{\partial p}{\partial r} = 0 \tag{1.1}$$

$$\frac{\partial v}{\partial t} + \frac{1}{r} \frac{\partial p}{\partial \theta} = 0 \tag{1.2}$$

$$\frac{\partial p}{\partial t} + \frac{\partial u}{\partial r} + \frac{1}{r} \frac{\partial v}{\partial \theta} + \frac{u}{r} = S(r, \theta, t)$$
(1.3)

where p is the pressure, and u and v are the velocities in the r and θ directions, respectively. The circular cylinder has a radius of 0.5 and centered at r = 0. The computational domain is as shown in Figure 1.

Equations (1.1)-(1.3) will be discretized by a hybrid of finite difference⁴ and Fourier spectral methods⁵ and time integration will be carried out by a optimized Runge-Kutta scheme⁶. In addition, numerical non-reflecting, or absorbing, boundary condition is needed for grid termination at the outer boundary. This is achieved by using the Perfectly Matched Layer technique^{1,2,3} in th present paper.

In what follows, we will first discuss the spatial and temporal discretization schemes used in solving (1.1)-(1.3). Then the absorbing boundary condition to be used at the far field is proposed and its efficiency is investigated. These are followed by the numerical results of Problems 1 and 2 and their comparisons with the exact solution whenever possible.

2.1 Discretization

2.1.1 Mesh

From numerical discretization point of view, it is convenient to use a mesh with fixed spacings Δr and $\Delta \theta$. However, such a mesh will not be desirable for the present problem for two reasons.

First, the grid points will be over concentrated near the cylinder while relatively sparse at the far field. Consequently, in order to resolve the waves at the far field, it will result in a needlessly dense grid distribution near the cylinder. Secondly, and perhaps more importantly, the overly dense mesh near the cylinder will reduce the CFL number and thus lead to a very small time step in explicit time integration schemes such as the Runge-Kutta schemes.

To increase the computational efficiency, a multi-domain polar grid system will be used, as shown in Figure 2. In this system, the number of grid points in the θ direction is different in each sub-domains. For instances, suppose that the entire computational domain is divided into 3 sub-domains and that there are M points in the θ direction of the inner most sub-domain, then $\Delta\theta$ will be taken as follows:

$$\Delta \theta = \frac{2\pi}{M} \quad \text{for} \quad 0.5 \le r < r_1 \tag{2.1}$$

$$\Delta \theta = \frac{2\pi}{M} \quad \text{for } 0.5 \le r < r_1$$

$$\Delta \theta = \frac{2\pi}{2M} \quad \text{for } r_1 \le r < r_2$$
(2.1)

$$\Delta\theta = \frac{2\pi}{4M} \quad \text{for} \quad r_2 \le r \le r_3 \tag{2.3}$$

The Spacing in r, Δr , will be fixed for all sub-domains.

2.1.2 Spatial discretization

The spatial derivatives will be discretized using a hybrid of finite difference (in r direction) and Fourier spectral (in θ direction) methods on the grid system described above. In particular, a 7-point 4-th order central difference scheme (as in the DRP scheme⁴) is used for the derivatives in the r direction. For grid points near the computational boundary where a central difference can not be applied, backward differences are used. For numerical stability with backward differences, a 11-point 10th order numerical filter is all applied in all the computations. The details are referred to ref [2]. This is largely a straightforward process. However, at any interface of two sub-domains, extra values are needed in the inner sub-domain for the stencils extended from the outer subdomain, as shown in Figure 3. These values are obtained by interpolation using Fourier expansion of the inner sub-domain values⁵.

2.1.3 Time integration

Time integration will be carried out using an optimized Low-Dissipation and Low-Dispersion Runge-Kutta (LDDRK) scheme⁶. The Runge-Kutta scheme is an explicit single-step multi-stage time marching scheme. Let the time evolution equation, after the spatial discretization, be written as

$$\frac{d\mathbf{U}}{dt} = F(\mathbf{U}, t) \tag{3}$$

where the right hand side is now time dependent when the forcing term is present. Then, a p-stage scheme advances the solution from \mathbf{U}^n to \mathbf{U}^{n+1} as follows:

1. For i = 1, 2, ..., p, compute $(\beta_1 = 0)$:

$$\mathbf{K}_{i} = \Delta t F(\mathbf{U}^{n} + \beta_{i} \mathbf{K}_{i-1}, t_{n} + \beta_{i} \Delta t)$$
(4.1)

2. Then

$$\mathbf{U}^{n+1} = \mathbf{U}^n + \mathbf{K}_p \tag{4.2}$$

The optimized coefficients β_i are given in ref [6]. In particular, the LDDRK 5-6 scheme is used in all the computations.

2.2 Perfectly Matched Layer

At the far field boundary, non-reflective boundary condition is needed to terminate the grids. In the present paper, we introduce a Perfectly Matched Layer around the outer boundary for this purpose, so that the out-going waves are absorbed in the added Perfectly Matched Layer domain while giving very little reflection to the interior domain.

The Perfectly Matched Layer equations to be used in the absorbing region will be constructed by splitting the pressure p into two variables p_1 and p_2 and introducing the absorption coefficients. This results in in a set of modified equations to be applied in the added absorbing layer. The following PML equations are proposed:

$$\frac{\partial u}{\partial t} + \sigma_r u = -\frac{\partial p}{\partial r} \tag{5.1}$$

$$\frac{\partial v}{\partial t} = -\frac{1}{r} \frac{\partial p}{\partial \theta} \tag{5.2}$$

$$\frac{\partial p_1}{\partial t} + \sigma_r p_1 = -\frac{\partial u}{\partial r} \tag{5.3}$$

$$\frac{\partial p_2}{\partial t} = -\frac{1}{r} \frac{\partial v}{\partial \theta} - \frac{u}{r} \tag{5.4}$$

in which $p = p_1 + p_2$ and σ_r is the absorption coefficient. We note that when $\sigma_r = 0$, (5.1)-(5.4) reduce to the Euler equations (1.1)-(1.3).

The above PML equations are easy to implement in finite difference schemes since the spatial derivative in r involves only the total pressure p, which is available in both the interior and PML domains. Thus the difference operator can be applied across the interface of the interior and PML domains in a straight forward manner. Inside the PML domain, the value of σ_r is increased gradually since a wide stencil has been used in the finite difference scheme. In particular, σ_r varies as

$$\sigma_r = \sigma_m \left(\frac{r - r_o}{D}\right)^{\beta} \tag{6}$$

where D is the thickness of the PML domain and r_o is the location of the interface between the interior and PML domain.

2.3 Numerical results

2.3.1 Results of Problem 1

In Problem 1, a time periodic acoustic source is located at $(r, \theta) = (4, 0)$. The source term in equation (1.3) is given as

$$S(r, \theta, t) = \sin(\omega t)e^{-(\ln 2)[(r\cos\theta - 4)^2 + (r\sin\theta)^2]/0.2^2}$$

where $\omega = 8\pi$.

For the results presented below, the grid spacing in radial direction is $\Delta r = 0.03125$ and the mesh is terminated at $r_{max} = 13.0$. This results in 401 points in the r direction. The computational domain of $r \times \theta = [0.5, 13] \times [0, 2\pi]$ is divided into 3 sub-domains with the r range as [0.5, 1.5), [1.5, 3) and [3, 13] respectively. The value of $\Delta\theta$ in each sub-domain is as shown below:

$$\Delta \theta = \frac{2\pi}{90}$$
 for $0.5 \le r < 1.5$

$$\Delta \theta = \frac{2\pi}{180}$$
 for $1.5 \le r < 3.0$

$$\Delta \theta = \frac{2\pi}{360}$$
 for $3.0 \le r \le 13.0$

This yields a mesh with 135480, or approximately 351², total grid points.

The time integration is carried out by an optimized Low-Dissipation and Low-Dispersion Runge-Kutta scheme as detailed in section 2.1.3. The time step is $\Delta t = 0.02083$.

A PML domain of 16 grid points in the radial direction is used around the outer boundary. That is, the Euler equations (1.1)-(1.3) are used for $0.5 \le r < 12.5$ and the PML equations (5.1)-(5.4) are used for $12.5 \le r < 13.0$. σ_r varies as given in (6) with $\sigma_m \Delta r = 2$ and $\beta = 2$.

Figure 4 shows instantaneous pressure contours at t=30. The resolution of the grid system is about 8 points per wavelength. To assess the effectiveness of the absorbing boundary condition, the pressure history was also monitored at a set of selected locations near the PML domain. Figure 5(a)-(c) plot the pressure as a function of time at r=11.6875 and $\theta=0$, $\pi/2$ and π , respectively. It is seen that the pressure history first shows large initial transient generated by the startup of the source term. However, after the transient has passed the monitoring points, time periodic responses are observed. We point out that the periodic oscillations had much smaller magnitudes compared with the transient and, yet, the time periodic state is established very quickly after the transient signal. This indicates that the absorbing boundary condition is quite effective and the reflection is indeed very small. The reflection error will be further quantified in problem 2.

The directivity pattern of the acoustic field is shown in Figure 6 where \bar{p}^2 was computed as

$$\bar{p}^2 = \frac{1}{T} \int_{t_0}^{t_0 + T} p^2 dt$$

where $t_0 = 25$ and T = 1 has been used, which includes four periods. Also shown in Figure 6 is the exact solution in dotted line. Excellent agreement is observed.

2.3.2 Results of Problem 2

In problem 2, the source term in (1.3) is not present, i.e. $S(r, \theta, t) = 0$, and the acoustic field is initialized with a pressure pulse given as

$$p = e^{-(\ln 2)[(r\cos\theta - 4)^2 + (r\sin\theta)^2]/0.2^2}, \quad u = v = 0$$

For the results presented below, $\Delta r = 0.05$ and the mesh is truncated at $r_{max} = 8.5$. Thus the number of grid points in the r direction is 161. Again, the computational domain is divided into three sub-domains and the values of $\Delta\theta$ are

$$\Delta\theta = \frac{2\pi}{64} \quad \text{for} \quad 0.5 \le r < 1.5$$

$$\Delta\theta = \frac{2\pi}{128} \quad \text{for} \quad 1.5 \le r < 3.0$$

$$\Delta\theta = \frac{2\pi}{256} \quad \text{for} \quad 3.0 \le r \le 8.5$$

This yields a mesh with 33536, or approximately 183^2 , total grid points. Time step is $\Delta t = 0.03125$.

Figure 7 shows the instantaneous pressure contours at select times. The out-going waves are absorbed in the PML domain giving no visible reflection to the interior domain. A PML domain of 10 points in the radial direction is used for this problem. Thus the domain where the PML equations are applied is for $8 < r \le 8.5$. Pressure responses at three chosen locations are shown in Figure 8.

To further quantify the numerical reflection error at the artificial boundary, the current solution is compared with a reference solution. The reference solution is computed using a larger computational domain so that its solution is not affected by the grid truncation. The differences of the computed solutions using PML domains and the reference solution are plotted in Figure 9. We observe that, first, the reflection errors are small when PML domains of 10 or more points are used. Second, the reflection errors, however, does not show order-of-magnitude improvements as the thickness of PML domain increases. This is a different behavior as compared to that of Cartesian PML equations^{1,2,3}.

3. CATEGORY 2 — PROBLEM 2

In this problem, CAA technique is applied to compute sound radiation from a circular duct (Figure 10). The progressive duct wave mode is specified at the duct inlet and the radiated sound field is to be calculated. In particular, sound directivity pattern and pressure envelope inside the duct are to be determined. For the given problem, the duct mode has been chosen to be axisymmetric.

In cylindrical coordinates (x, r, θ) , the Linearized Euler Equations for the axisymmetric disturbances are

$$\frac{\partial u}{\partial t} + \frac{\partial p}{\partial x} = 0 \tag{7.1}$$

$$\frac{\partial v}{\partial t} + \frac{\partial p}{\partial r} = 0 \tag{7.2}$$

$$\frac{\partial p}{\partial t} + \frac{\partial u}{\partial x} + \frac{\partial v}{\partial r} + \frac{v}{r} = 0 \tag{7.3}$$

where p is the pressure, u and v are the velocities in the x and r directions respectively.

As in the previous section, the spatial derivatives will be discretized by the 7-point 4th-order central difference scheme and the time integration will be carried out by the LDDRK 5-6 scheme. These are the same as those used for the First Workshop Problems, ref [7], including the solid wall and centerline treatments. The emphasis of this section will be on the implementation of the non-reflective boundaries in the current problem.

There are two types of non-reflective boundaries encountered in the present problem, as shown in Figure 10. One is the far field non-reflecting boundary condition for the termination of grids. The numerical boundary condition should be such that the out-going waves are not reflected. The second type is the inflow boundary condition at the duct inlet. At the inlet of the duct, we wish to feed-in the progressive duct mode and at the same time absorb the waves reflected from the open end of the duct. In the present paper, both types of non-reflective boundary conditions are implemented using the Perfectly Matched Layer technique. The details are given below.

3.1 PML absorbing boundary condition

To absorb the out-going waves, we introduce a PML domain around the outer boundary of the computational domain, similar to that used in the previous section only that the form of PML equations will be different. For the linearized Euler equations (7.1)-(7.3) in cylindrical coordinates, we proposed the following PML equations:

$$\frac{\partial u}{\partial t} + \sigma_x u = -\frac{\partial p}{\partial x} \tag{8.1}$$

$$\frac{\partial v}{\partial t} + \sigma_r v = -\frac{\partial p}{\partial r} \tag{8.2}$$

$$\frac{\partial p_1}{\partial t} + \sigma_x p_1 = -\frac{\partial u}{\partial x} \tag{8.3}$$

$$\frac{\partial p_2}{\partial t} + \sigma_r p_2 = -\frac{\partial v}{\partial r} - \frac{v}{r} \tag{8.4}$$

where $p = p_1 + p_2$ and the absorption coefficients σ_x and σ_r have been introduced for absorbing the waves that enter the PML domain. The above form follows the PML equations for the Cartesian coordinates given in refs [1, 2]. Here we need only to split the pressure since no mean flow is present. We note that, the Euler equations (7.1)-(7.3) can be recovered from the PML equations (8.1)-(8.4) with $\sigma_x = \sigma_r = 0$ by adding the split equations. Consequently, the interior domain where the Euler equations are applied is regarded as absorption coefficients being zero.

The absorption coefficients σ_x and σ_r are *matched* in a special way, namely, σ_x will remain the same across a horizontal interface and σ_r will remain the same across a vertical interface, as

shown in Figure 11 and described in detail in ref [1, 2]. Within the PML domain, σ_x or σ_r are increased gradually as discussed in the previous section.

3.2 Inflow Boundary Condition

At the inlet of the duct, we wish to feed-in the progressive duct modes and at the same time absorb the waves reflected from the open end of the duct, as shown in Figure 12. For this purpose, a PML domain is also introduced at the inlet. In this region, referred to as the *inflow-PML domain*, we treat the solution as a summation of the incoming and out-going waves and apply the PML equations (8.1)-(8.4) to the out-going part. That is, we express and store the variables as

$$\begin{pmatrix} u \\ v \\ p \end{pmatrix} = \begin{pmatrix} u_{in} \\ v_{in} \\ p_{in} \end{pmatrix} + \begin{pmatrix} u' \\ v' \\ p' \end{pmatrix} \tag{9}$$

in which u_{in} , v_{in} , and p_{in} are the "incoming wave", traveling to the right, and u', v', and p' are the "out-going" wave, reflected from the open end and traveling to the left. Since the incoming wave satisfies the linearized Euler equation, it follows that the out-going reflected wave will also satisfy (7.1)-(7.3). To absorb the "out-going" part in the inflow-PML domain, we apply the PML equations (8.1)-(8.4) to the reflected waves. This results in following equations for u', v' and p':

$$\frac{\partial u'}{\partial t} + \sigma_x u' = \frac{\partial p}{\partial x} - \frac{\partial p_{in}}{\partial x} \tag{10.1}$$

$$\frac{\partial v'}{\partial t} + \sigma_r v' = \frac{\partial p}{\partial r} - \frac{\partial p_{in}}{\partial r}$$
(10.2)

$$\frac{\partial p_1'}{\partial t} + \sigma_x p_1' = \frac{\partial u}{\partial x} - \frac{\partial u_{in}}{\partial x}$$
 (10.3)

$$\frac{\partial p_2'}{\partial t} + \sigma_r p_2' = \frac{\partial v}{\partial r} - \frac{\partial v_{in}}{\partial r} + \frac{v}{r} - \frac{v_{in}}{r}$$
(10.4)

where $p' = p'_1 + p'_2$ and u, v, p are those given in (9). Since the inflow-PML domain involves only a vertical interface between the interior and PML domains, it results in $\sigma_r = 0$ in (10.1)-(10.4). The right hand sides of (10.1)-(10.4) have been written in such a way that they can be readily evaluated in finite difference schemes. In particular, we note that, first, since the incoming wave is known, there should be no difficulty in computing their spatial derivatives. Second, the other spatial spatial derivative terms involve only the total u, v and p which are available in the interior domain as well as the inflow-PML domain by using (9).

3.3 Numerical Results

For the results given below, the computational domain is $x \times r = [-9, 9] \times [0, 9]$ in the cylindrical coordinate system. The duct centerline is at r = 0 and the radius of the duct is unity. The open end of the duct is located at x = 0. For both the low and high frequency cases, we have used a uniform grid with $\Delta x = \Delta r = 0.05$. This results in a 361 × 181 grid system. The time step that ensures both accuracy and stability is $\Delta t = 0.0545$ in the LDDRK 5-6 scheme.

To absorb the out-going waves at the far field, PML domains with a width of 10 grid points are used around the outer boundaries of the computational domain. In addition, an inflow-PML domain is employed at the duct inlet with the same width as in the far field.

Figure 13 shows the instantaneous pressure contours at t = 87.2 and $\omega = 7.2$ (low frequency case). It is seen that the waves decay rapidly in the PML domain. As in the previous section, the pressure as a function of time is monitored at a set of chosen points. Figure 14 shows the pressure histories at two points near the interior-PML interfaces (x, r) = (8, 0), (0, 8), and two points inside the duct (x, r) = (-2, 0), (-4.5, 0). We observe that, while the pressure responses at the far field quickly become time periodic after the initial transients have passed, it takes a longer time for the pressure inside the duct to reach the periodic state. This is believed to be due to the reflection of the transient at the open end of the duct which has to be absorbed by the inflow-PML domain before a periodic state can be established.

Numerical reflection error has also been assessed by comparing the computed solution using PML absorbing boundary condition to a reference solution using a larger computational domain. The maximum difference of the two solutions around the outer boundaries is plotted in Figure 15 for n = 10 and 20 where n is the width of the PML domain used. It is seen that satisfactory results are obtainable with a width of 10 points and the reflection error is further reduced significantly by increase the width of the PML domain.

Figure 16 shows the directivity pattern of the radiated sound field. The envelopes of the pressure distribution inside the duct are given in Figure 17. Results for the high frequency case, $\omega = 10.3$, are shown in Figures 18-21.

4. CATEGORY 3

In this category, CAA technique is applied to a turbomachinery problem in which the sound field generated by a gust passing through a cascade of flat plates is to be computed directly from the time-dependent Euler equations :

$$\frac{\partial u}{\partial t} + M \frac{\partial u}{\partial x} + \frac{\partial p}{\partial x} = 0 \tag{11.1}$$

$$\frac{\partial v}{\partial t} + M \frac{\partial v}{\partial x} + \frac{\partial p}{\partial y} = 0 \tag{11.2}$$

$$\frac{\partial p}{\partial t} + M \frac{\partial p}{\partial x} + \frac{\partial u}{\partial x} + \frac{\partial v}{\partial y} = 0$$
 (11.3)

where M is the Mach number of the mean flow. In the above, the velocities have been non-dimensionalized by the speed of sound a_o and pressure by $\rho_o a_o^2$ where ρ_o is the density scale. The problem configuration is as shown in Figure 22. In non-dimensional scales, the chord length and the gap-to-chord ratio are both unity. In addition, periodicity is assumed for the top and bottom boundaries. A uniform mean flow is present which has a Mach number of 0.5. The

incident vortical gust is given as

$$u_{in} = -\frac{V_g \beta}{\alpha} \cos(\alpha x + \beta y - \omega t)$$
 (12.1)

$$v_{in} = V_g \cos(\alpha x + \beta y - \omega t) \tag{12.2}$$

$$p_{in} = 0 ag{12.3}$$

where $V_g = 0.005$.

In all three problems posed in this category, the sound field scattered by the plates as well as the loadings on the plates are to be determined. In Problem 1, the solutions are to be calculated by using a frozen gust assumption. In problem 2, the convected gust is to be simulated together with the scattered sound field. In problem 3, a sliding interface is introduced and the grids down stream of the interface are moving vertically with a given speed V_s . Problems in this category include several important and challenging issues in developing CAA techniques, such as the inflow and out flow conditions, solid boundaries and moving zones. In the present paper, the inflow and outflow conditions are implemented by the PML technique. The details of the boundary conditions as well as the sliding zone treatments are described below.

4.1 Outflow condition

At the downstream outflow boundary, the out-going waves consist of the acoustic waves scattered from the plates and the vorticity waves convected by the mean flow. To absorbed these waves with as little reflection as possible, a PML domain is used at the outflow boundary. For the linear Euler equations (11.1)-(11.3) with a uniform mean flow in the x direction, the following equations are applied in the added PML domain:

$$\frac{\partial u}{\partial t} + \sigma_x \, u = -M \frac{\partial u}{\partial x} - \frac{\partial p}{\partial x} \tag{13.1}$$

$$\frac{\partial v_1}{\partial t} = -\frac{\partial p}{\partial y} \tag{13.2}$$

$$\frac{\partial v_2}{\partial t} + \sigma_x \, v_2 = -M \frac{\partial p}{\partial x} \tag{13.3}$$

$$\frac{\partial p_1}{\partial t} + \sigma_x \, p_1 = -M \frac{\partial p}{\partial x} + \frac{\partial u}{\partial x} \tag{13.4}$$

$$\frac{\partial p_2}{\partial t} = -\frac{\partial v}{\partial y} \tag{13.5}$$

where v and p have been split into v_1 , v_2 and p_1 , p_2 , i.e., $v = v_1 + v_2$ and $p = p_1 + p_2$. Note that, since now the top and bottom boundaries are periodic, only one absorption coefficient, σ_x , is needed. In addition, the u velocity may not be split. For the Cartesian coordinates, it has been shown that the PML domain so constructed is reflectionless for all the linear waves supported by the Euler equations and the waves that enter the PML domain decay exponentially. The details are referred to ref. [1, 2].

4.2 Inflow condition

At the inflow, two types of waves co-exist, namely, the downstream propagating vorticity waves (the gust) and the upstream propagating acoustic waves (scattered from the plates). A successful inflow condition should simulate the downstream connection of the vorticity waves and at the same time be non-reflective for the upstream acoustic waves. As in the previous section (category 2), the inflow condition is implemented by introducing a PML domain at the inflow boundary. In the inflow-PML domain, the variables u, v and p are expressed and stored as a summation of the "incoming" vorticity wave and "out-going" acoustic waves as those given in (9). The incoming wave u_{in} , v_{in} and p_{in} is as given in (12.1)-(12.3). The PML equations (13.1)-(13.5) are then applied to the "out-going" waves u', v' and p'. Thus, in the inflow-PML domain, we solve

$$\frac{\partial u'}{\partial t} + \sigma_x u' = -M \frac{\partial u}{\partial x} - \frac{\partial p}{\partial x} + M \frac{\partial u_{in}}{\partial x} + \frac{\partial p_{in}}{\partial x}$$
(14.1)

$$\frac{\partial v_1'}{\partial t} = -\frac{\partial p}{\partial y} + \frac{\partial p_{in}}{\partial y} \tag{14.2}$$

$$\frac{\partial v_2'}{\partial t} + \sigma_x \, v_2' = -M \frac{\partial p}{\partial x} + M \frac{\partial p_{in}}{\partial x} \tag{14.3}$$

$$\frac{\partial p_1'}{\partial t} + \sigma_x \, p_1' = -M \frac{\partial p}{\partial x} - \frac{\partial u}{\partial x} + M \frac{\partial p_{in}}{\partial x} - \frac{\partial u_{in}}{\partial x} \tag{14.4}$$

$$\frac{\partial p_2'}{\partial t} = -\frac{\partial v}{\partial y} + \frac{\partial v_{in}}{\partial y} \tag{14.5}$$

Again, the right hand sides have been written in a way that the spatial derivatives can be readily evaluated in finite difference schemes. The implementation of above is similar to that in section 3.2.

4.3 Sliding Zone Treatments

In problem 3, a sliding interface is added to the computational domain and the grids downstream of the sliding interface is moving vertically with a speed V_s , Figure 23. That is, after each time step, the grids in the sliding zone advance vertically by $V_s\Delta t$. Due to this movement, the grids in the two zones are not necessary aligned in the horizontal direction. This will obviously give rise to difficulties in finite difference schemes when the stencils extend across the interface. Extra grid points are created as shown in Figure 24. In the present paper, values of variables on these points are obtained by interpolation using Fourier expansions in the vertical direction. For instance, let the values of pressure p on the regular grids be denoted as $p(j\Delta x, k\Delta y)$. Then the values of p on a point $(j\Delta x, y)$, not on a regular grid point, will be computed as

$$p(j\Delta x, y) = \sum_{n=-N/2}^{N/2-1} \hat{p}_{jn} e^{i\frac{2\pi n}{L}y}$$

where \hat{p}_{jn} is the Fourier transform of $p(j\Delta x, k\Delta y)$ in the y direction and N is the number of grid points $(N=L/\Delta y)$. The Fourier expansions are implemented efficiently using FFT. It is well known that Fourier interpolation is highly accurate, better than any polynomial interpolations. Indeed, we found that, using Fourier interpolation, the results with sliding zone (Problem 3) are virtually identical to those without a sliding interface (Problem 2).

4.4 Numerical Results

Since solutions of all three problems in this category are similar, we will concentrate on numerical results of Problem 2 in particular and present the results of Problems 1 and 3 as references.

4.4.1 Effectiveness of the inflow-PML boundary condition

We first demonstrate the validity and effectiveness of the inflow-PML boundary condition described in section 4.2 by a numerical example plane wave simulation. In this example, a plane vorticity wave, convecting with the mean flow, will be simulated. The computational domain is the same as that of problem 2 except that now no plate is present. The flow field is initialized as follows:

At
$$t=0$$
:
$$u=-\frac{V_g\beta}{\alpha}\cos(\alpha x+\beta y-\omega t)H(x+1)$$

$$v=V_g\cos(\alpha x+\beta y-\omega t)H(x+1)$$

$$p=0$$

where H(x) is a step function which has a value of zero for x > 0 and unity for x < 0.

Figure 25 shows instantaneous pressure contours at the initial state t=0 and subsequent moments at t=4.8 and 14.4. The inflow-PML domain described in 4.2 is applied at the inflow boundary. It is seen that a plane vorticity wave is established. Figure 26 shows the v-velocity and pressure as functions of time at a point (x,y)=(-2,0). Notice that while the velocity is periodic, the pressure is not exactly zero as a plane vorticity wave should behave. This is due to our initial flow field being not exact along the cut-off line x=-1 which generates small pressure waves. Although these pressure waves are eventually absorbed by the PML domains at both the inflow and out-flow boundaries, the decay of the pressure is slow due to periodicity of the top and bottom boundaries. However, the magnitude of these pressure waves is small as shown in Figure 25.

Simulation of a plane acoustic wave has also been performed with similar results.

4.4.2 Low frequency gust

For the low frequency case, $\omega = 5\pi/4$, $\alpha = \beta = 5\pi/2$. The computational domain is $[-3.5, 4.5] \times [0, 4]$. A uniform grid with $\Delta x = \Delta y = 0.05$ is used and time step used is $\Delta t = 0.044$. The PML domains contain 20 points in the *x*-direction. Thus the interior domain in which the Euler equations are applied is $[-2.5, 3.5] \times [0, 4]$. Figure 27 shows the instantaneous pressure

and v-velocity contours. In the velocity contours, also visible is the trailing vorticity waves from the plates due to numerical viscosity in the finite difference scheme. The pressure intensity along x = -2 and x = 3 are shown in Figure 28, along with the results of Problems 1 and 3. Close agreement is found. Especially, results of Problems 2 and 3 are identical.

4.4.3 High frequency gust

For the high frequency case, $\omega = 13\pi/4$, $\alpha = \beta = 13\pi/2$. The computational domain is $[-3.5, 4.5] \times [0, 4]$ and $\Delta x = \Delta y = 0.03125$. Time step $\Delta t = 0.028$.

Pressure and v-velocity contours are shown in Figure 29. We point out that it appears that the out-going waves are not absorbed as efficiently as in the low frequency case as they enter the out-flow PML domain. However, the waves reflected from the end of the PML domain are absorbed more effectively so the solutions in the interior domain are not affected. Results for sound intensity are shown in Figure 30.

5. CONCLUSIONS

Problems in Categories 1, 2 and 3 have been solved by a finite difference method. Numerical schemes have been optimized for accuracy and efficiency. Perfectly Matched Layer technique for Euler equations have been successfully applied to all the problems as a general treatment for non-reflecting boundaries. It is demonstrated that the proposed PML technique is applicable to radiation boundaries as well as out-flow and inflow boundaries and can be effective for non-Cartesian grids. The accuracy and efficiency of the PML absorbing boundary conditions are also addressed.

Acknowledgment

This work was supported by the National Aeronautics and Space Administration under NASA contract NAS1-19480 while the authors were in the residence at the Institute for Computer Application in Science and Engineering, NASA Langley Research Center, VA 23665, USA.

References

- 1. F. Q. Hu, "On absorbing boundary conditions for linearized Euler equations by a Perfectly Matched Layer", *Journal of Computational Physics*, Vol 128, No. 2, 1996.
- 2. F. Q. Hu' "On perfectly matched layer as an absorbing boundary condition", AIAA paper 96-1664, 1996.
- 3. J-P Berenger, "A Perfect Matched Layer for the absorption of electromagnetic waves", *Journal of Computational Physics*, Vol 114, 185, 1994.
- 4. C. K. W. Tam and J. C. Webb, "Dispersion-relation-preserving schemes for computational acoustics" *Journal of Computational Physics*, Vol 107, 262-281, 1993.

- 5. C. Canuto, M. Y. Hussainin, A. Quarteroni and T. A. Zang, *Spectral Methods in Fluid Dynamics*, Springer-Verlag, 1988.
- 6. F. Q. Hu, M. Y. Hussaini, J. L. Manthey, "Low-dissipation and low-dispersion Runge-Kutta schemes for computational acoustics", *Journal of Computational Physics*, Vol 124, 177-191, 1996.
- 7. F. Q. Hu, M. Y. Hussaini, J. L. Manthey, "Application of low-dissipation and low-dispersion Runge-Kutta schemes to Benchmark Problems in Computational Aeroacoustics", *ICASE/LaRC Workshop on Benchmark Problems in Computational Aeroacoustics*, Hardin et al Eds, NASA CP 3300, 1995.

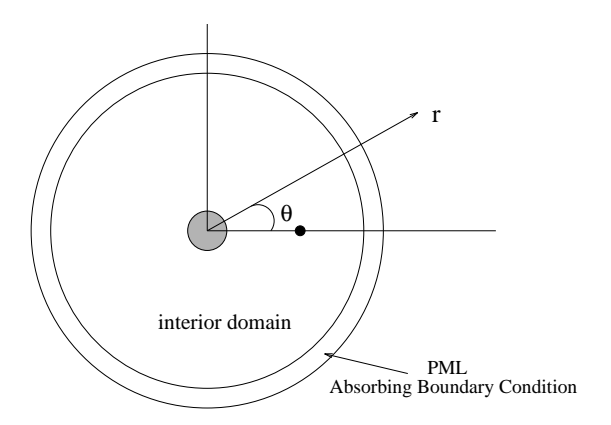


Figure 1. Schematic of the computational domain in cylindrical coordinates. A PML domain is introduced at outer boundary.

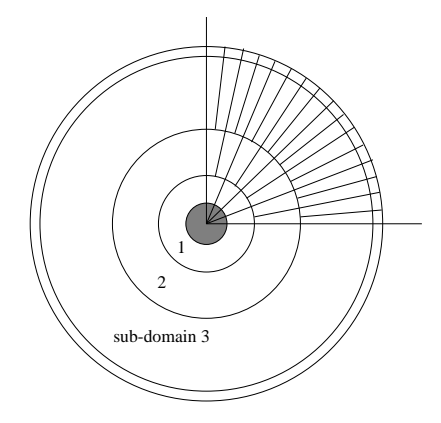


Figure 2. A schematic showing variable spacing in θ direction in sub-domains.

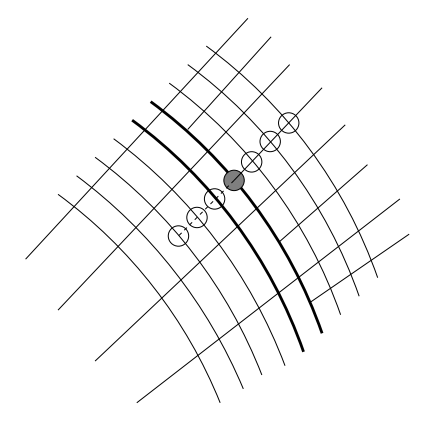


Figure 3. Extra values near the interface of sub-domains.

Figure 4. Instantaneous pressure contours. Problem 1.

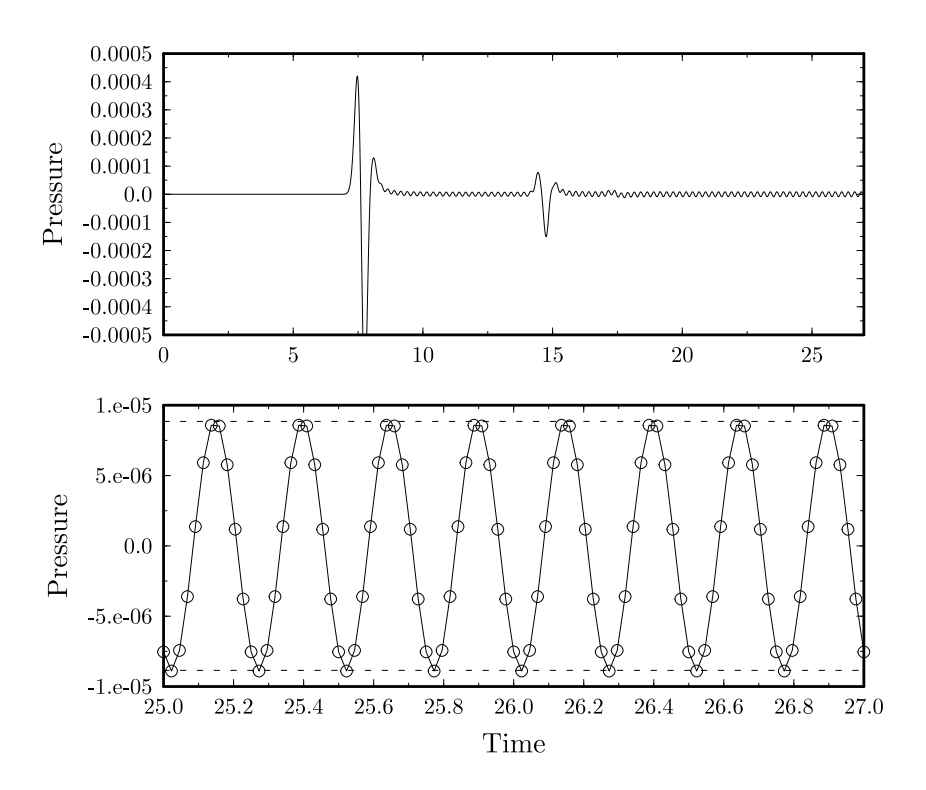


Figure 5a. Pressure as a function of time at r = 11.6875, $\theta = 0$.

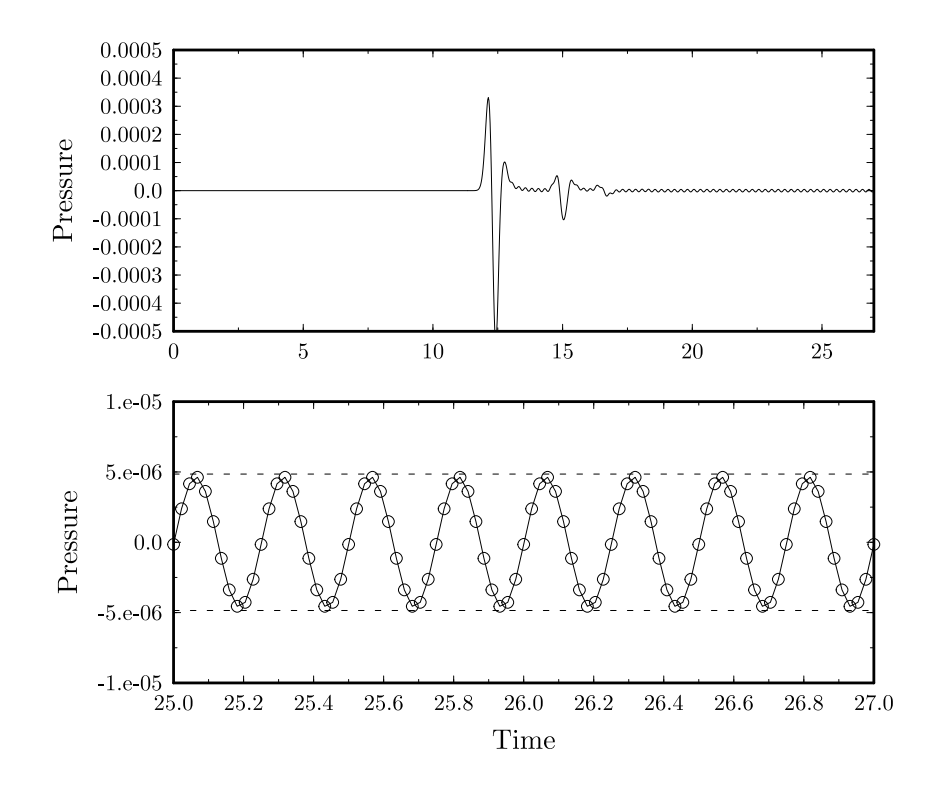


Figure 5b. Pressure as a function of time at r = 11.6875, $\theta = \pi/2$.

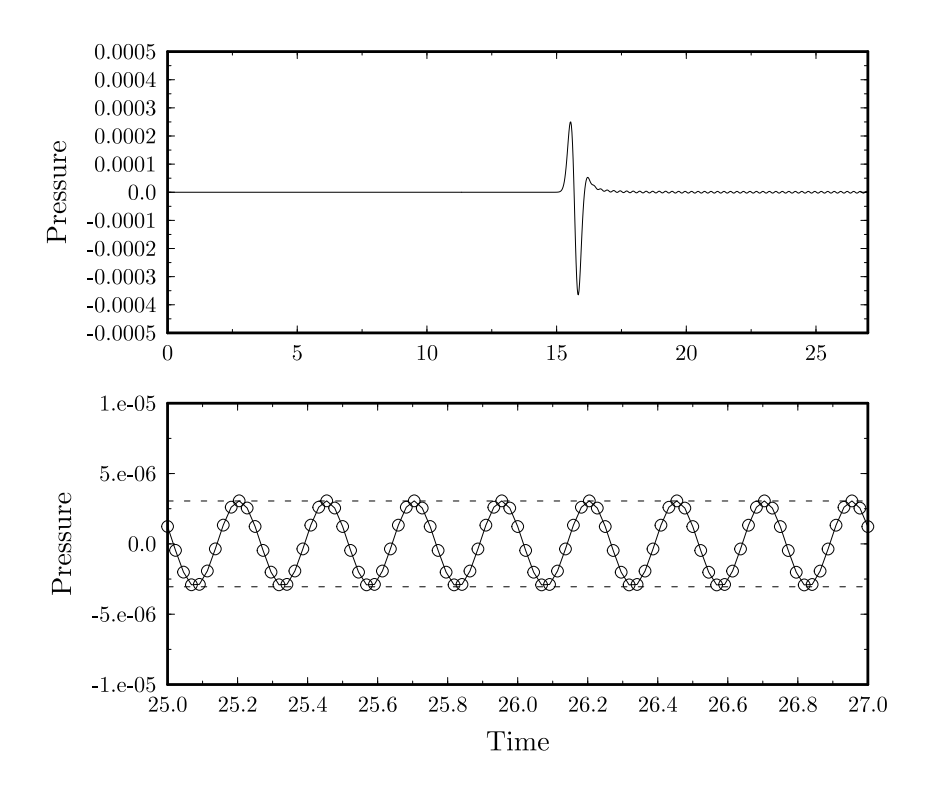


Figure 5c. Pressure as a function of time at $r=11.6875,\ \theta=\pi$

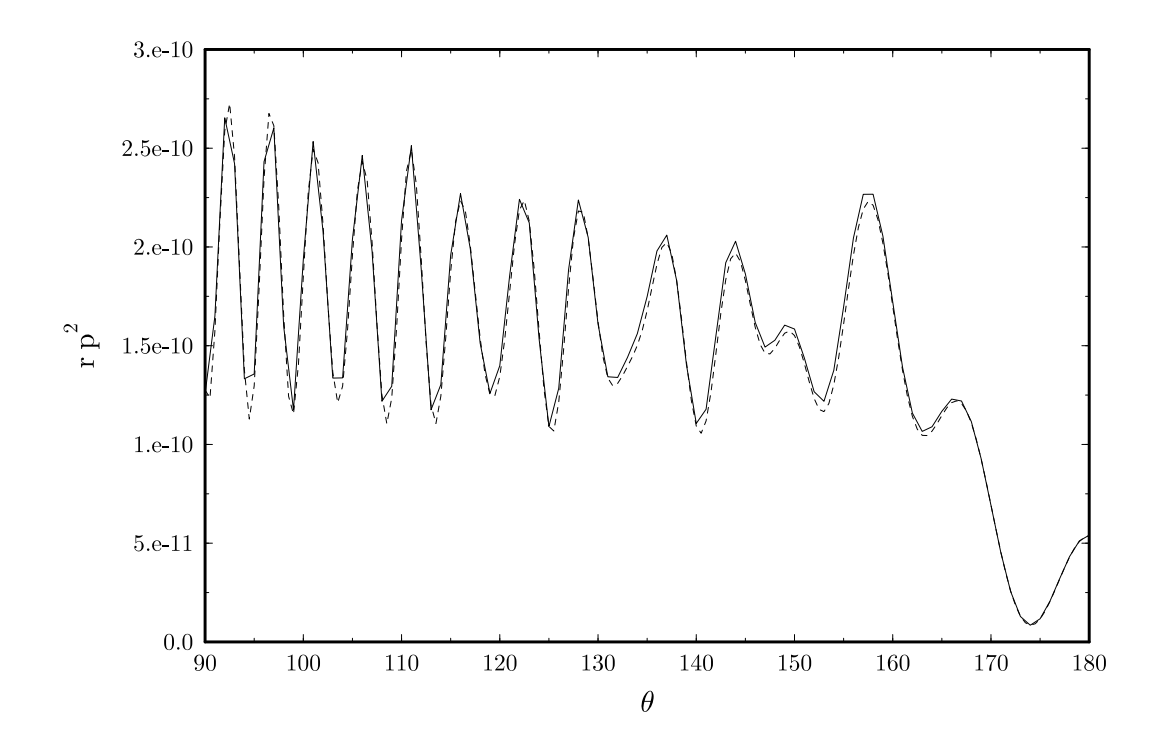


Figure 7a.

Figure 7b.

Figure 7c

Figure 7d.

Figure 7 Instantaneous Pressure contours. Problem 2. (a) t = 3; (b) t = 5; (c) t = 7; (d) t = 9.

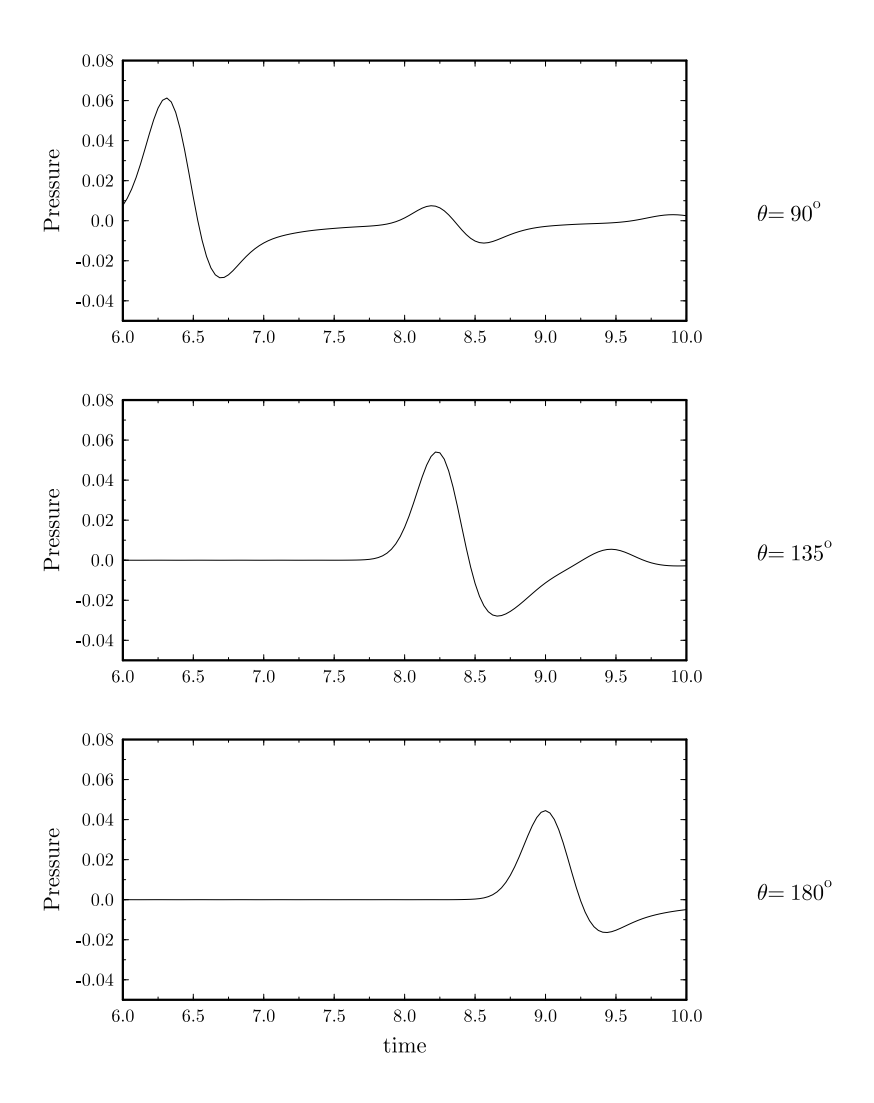


Figure 8. Pressure history at three chosen locations. r = 5.

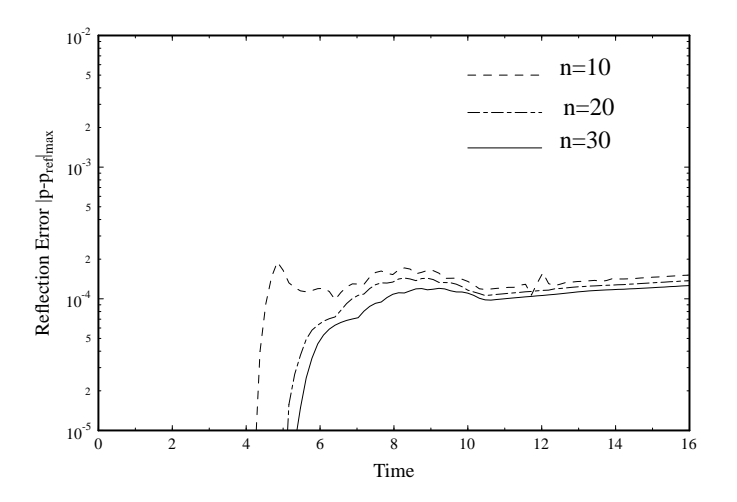


Figure 9. Maximum umerical reflection error as compared to a reference solution. The reference solution is obtained using a larger computational domain. Indicated are the width of PML domain.

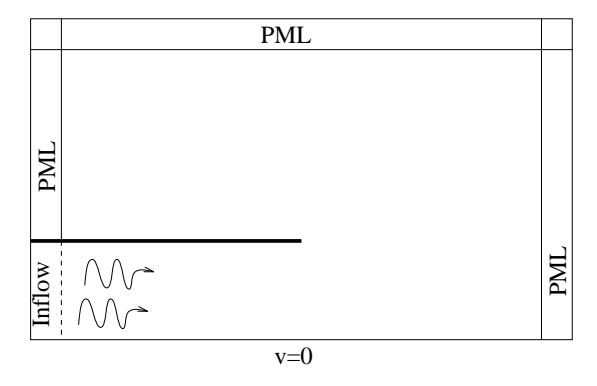


Figure 10. Schematic of the computational domain for Category 2, Problem 2. PML absorbing domains are introduced at the far field, as well as an inflow-PML domain at the inlet.

$ \begin{array}{c c} \sigma_{X} \neq 0 \\ \sigma_{\Gamma} \neq 0 \end{array} $	$\sigma_{\mathbf{X}} = 0$ $\sigma_{\mathbf{r}} \neq 0$	$ \begin{array}{c c} \sigma_{x} \neq 0 \\ \sigma_{r} \neq 0 \end{array} $	r
$\sigma_{\mathbf{X}} \neq 0$ $\sigma_{\mathbf{r}} = 0$	$\sigma_{X} = \sigma_{T} = 0$	$\sigma_{\mathbf{x}} \neq 0$ $\sigma_{\mathbf{r}} = 0$	r _p
	;	x _p	

Figure 11. Schematic of absorbing coefficients in the interior and PML domains.

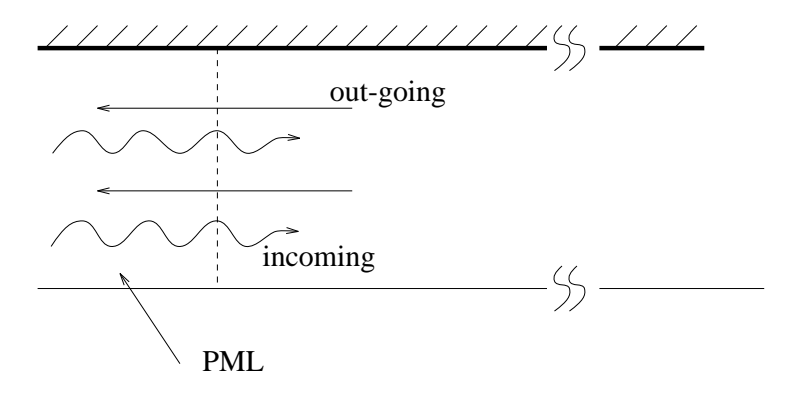


Figure 12. At the duct inlet, incoming and out-going waves co-exist. An inflow-PML domain is introduced inside the duct at the inlet to absorb the out-going wave only.

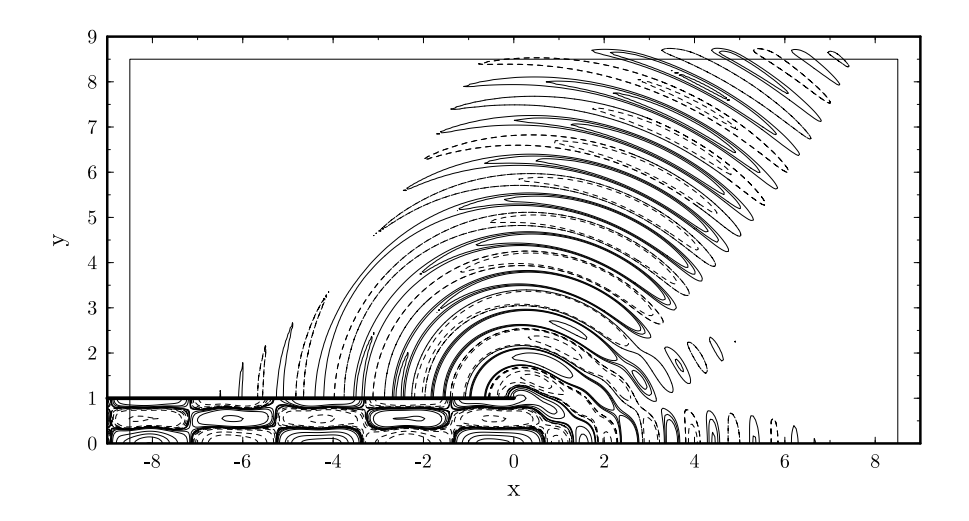


Figure 13. Pressure contours at t = 87.2, $\omega = 7.2$.

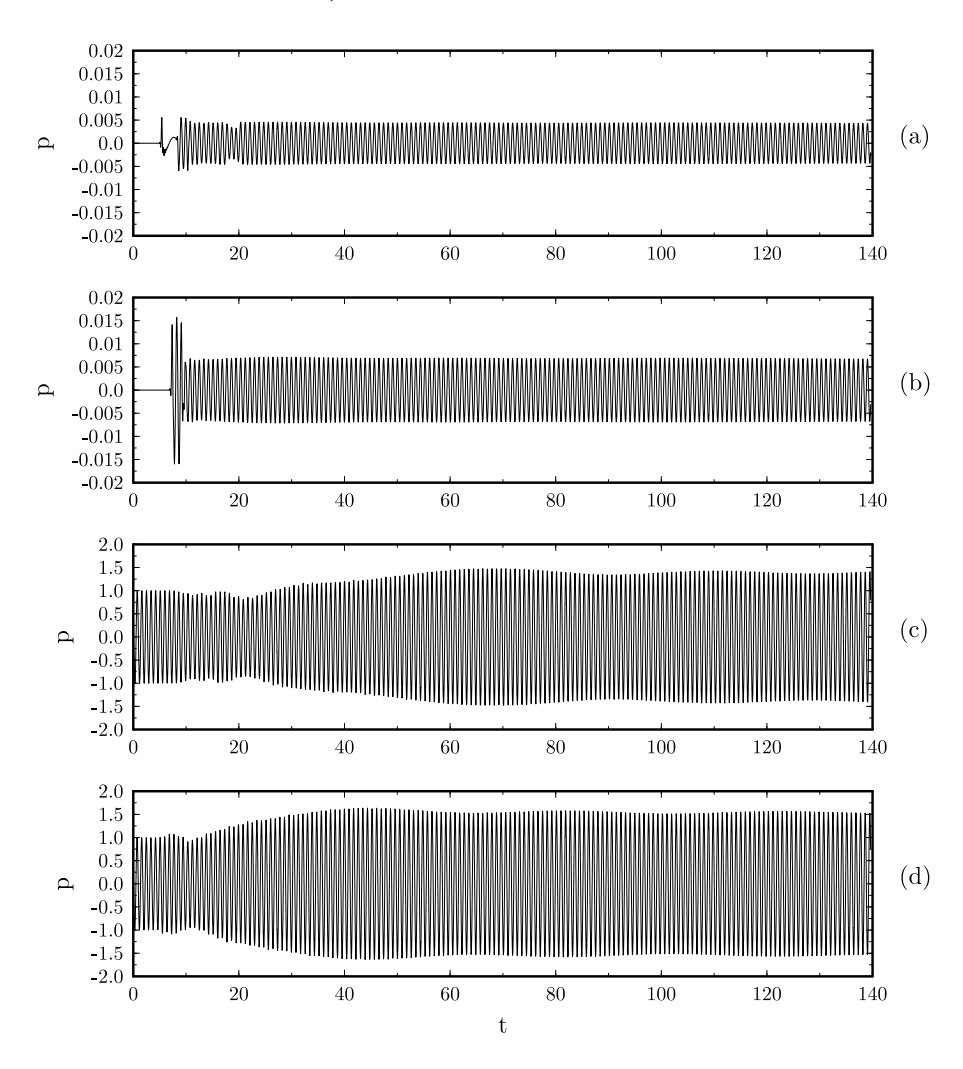


Figure 14. Pressure history at four locations, $\omega = 7.2$, (a) (x, r) = (8, 0), (b) (0, 8), (c) (-2, 0), (d) (-4.5, 0).

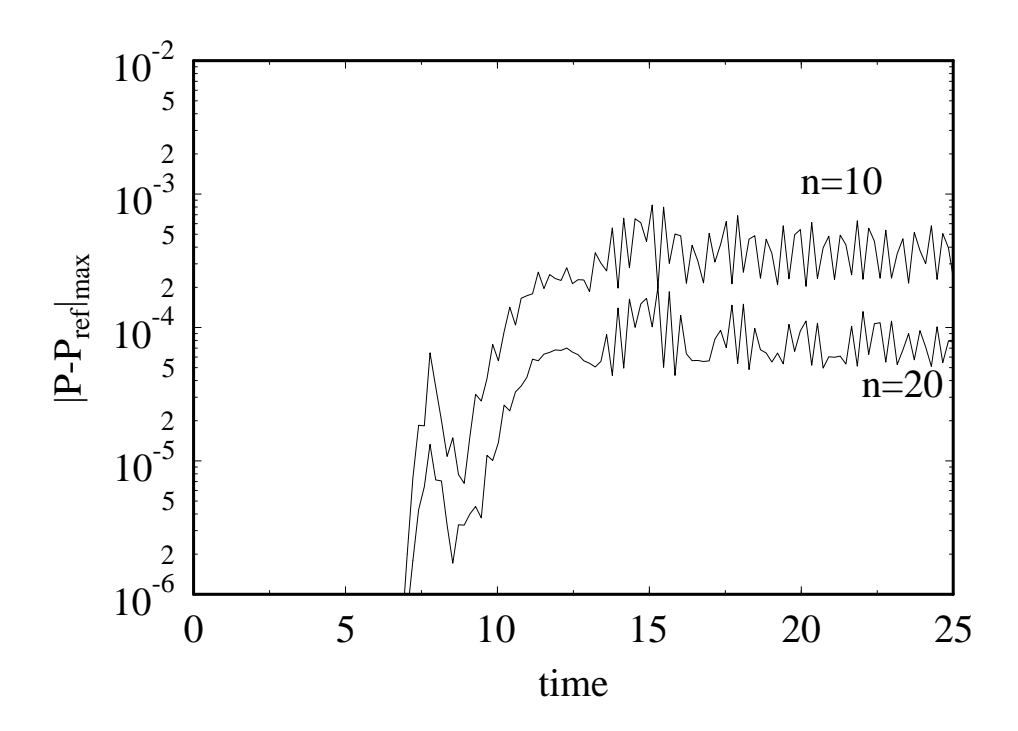


Figure 15. Maximum reflection error on the far field boundaries. The reference solution is obtained by using a larger computational domain. n indicates the width of the PML domain used.

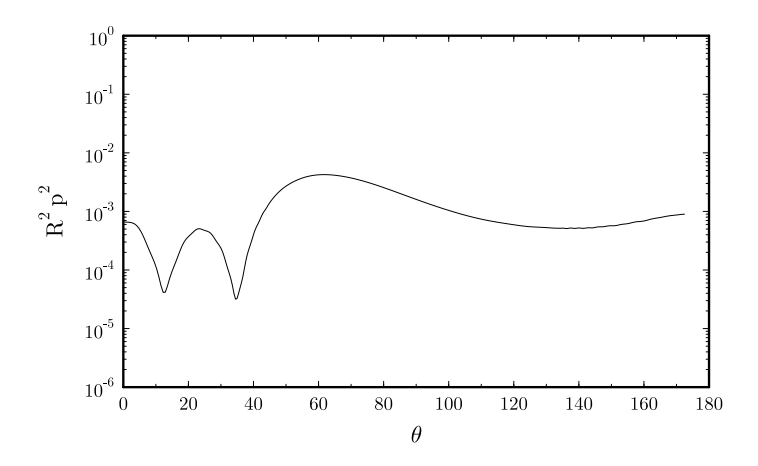


Figure 16. Directivity of radiated sound. $\omega = 7.2$.

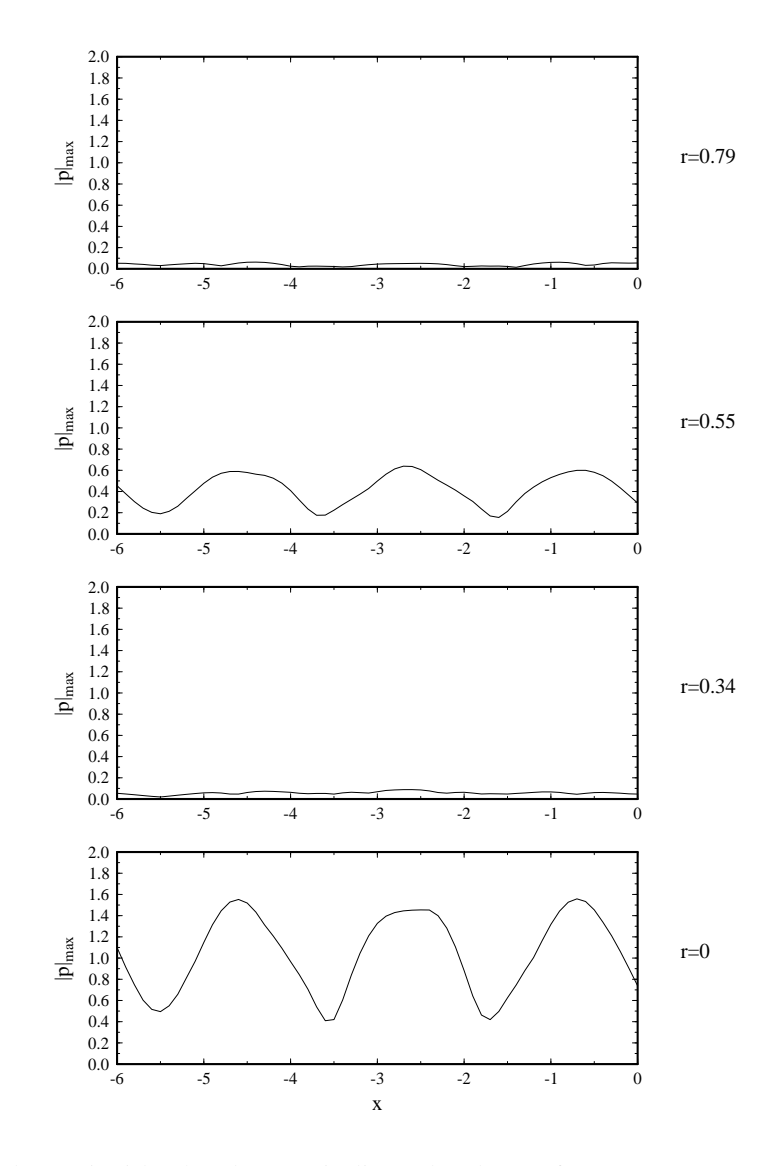


Figure 17. Pressure envelopes inside the duct at indicated values of r. $\omega = 7.2$

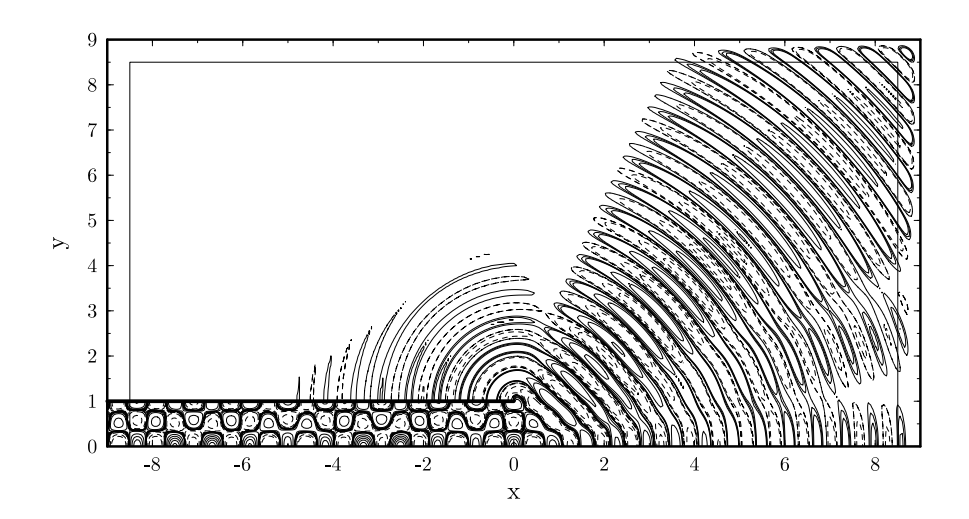


Figure 18. Pressure contours at t = 87.2, $\omega = 10.3$.

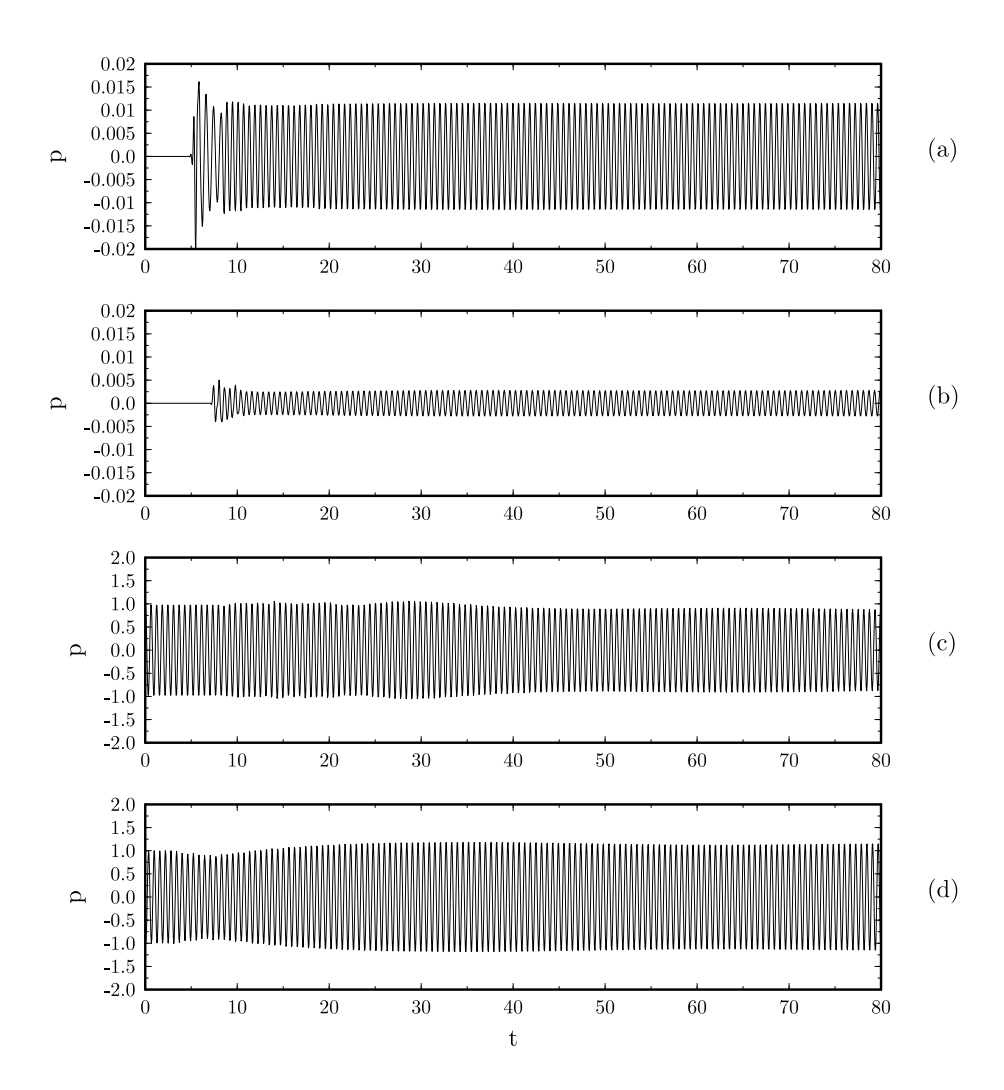


Figure 19. Pressure history at four locations, $\omega = 10.3$, (a) (x, r) = (8, 0), (b) (0, 8), (c) (-2, 0), (d) (-4.5, 0).

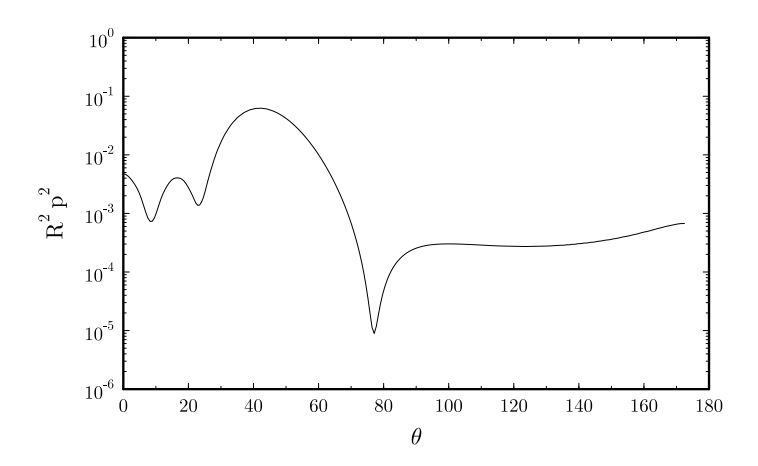


Figure 20. Directivity of radiated sound. $\omega = 10.3$.

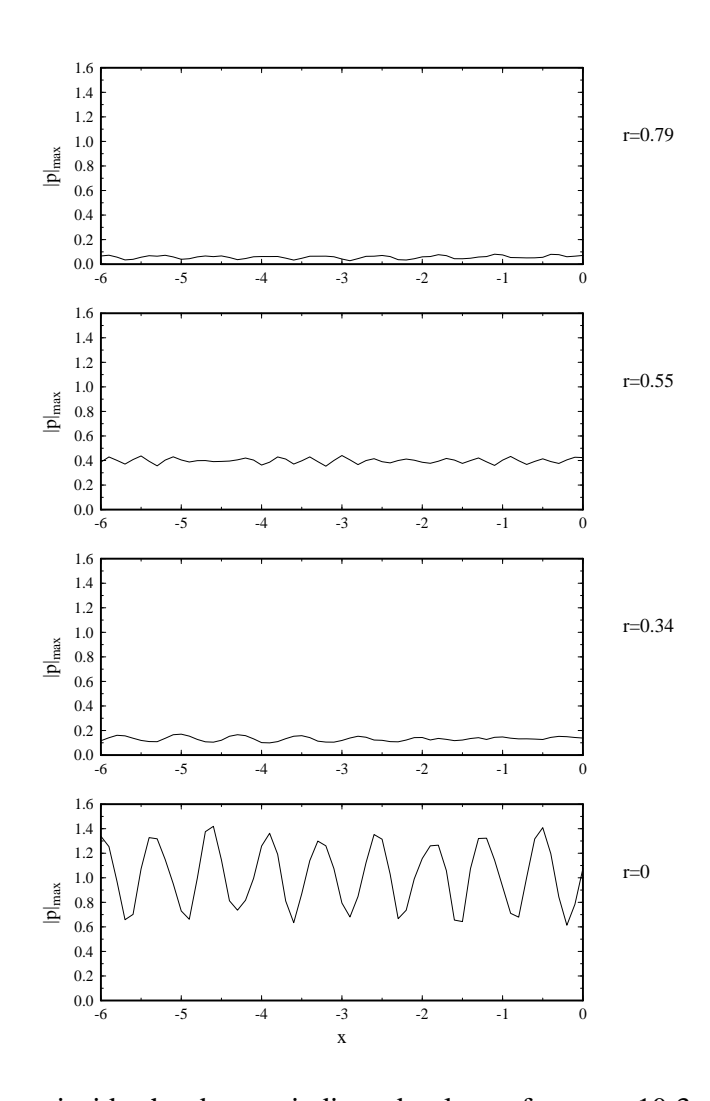


Figure 21. Pressure envelopes inside the duct at indicated values of r. $\omega = 10.3$

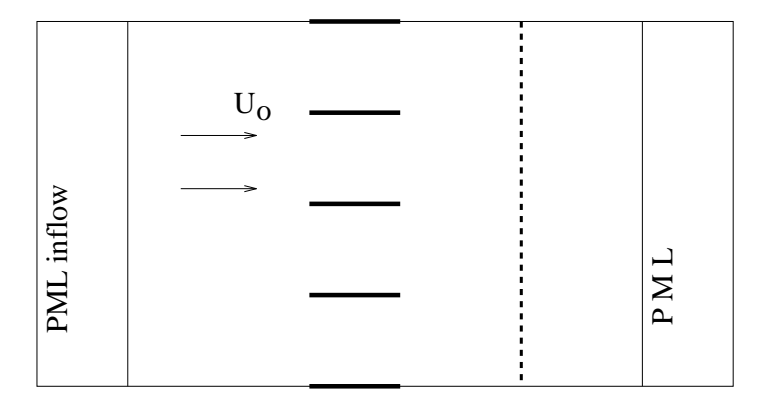


Figure 22. Schematic of the computational domain for Category 3.

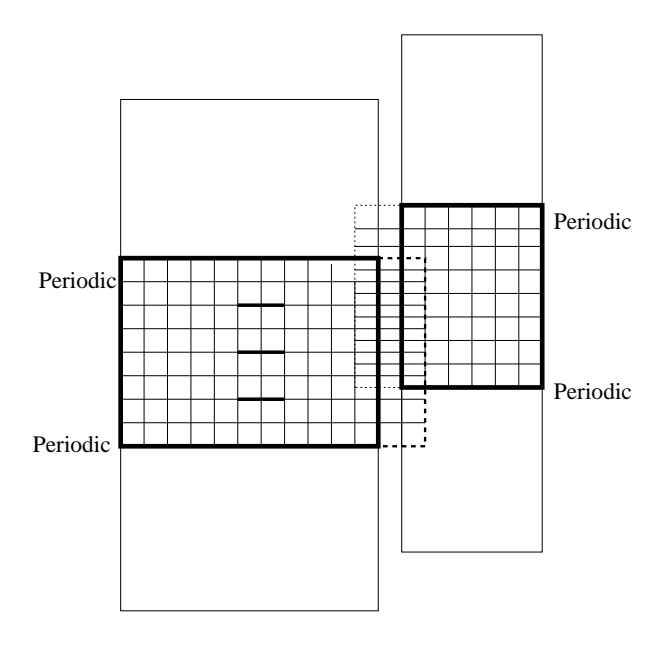


Figure 23. Sliding zone.

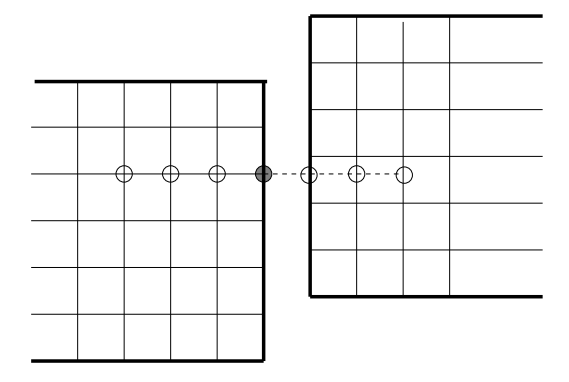


Figure 24. Extra grid points near the sliding interface for a central difference scheme.

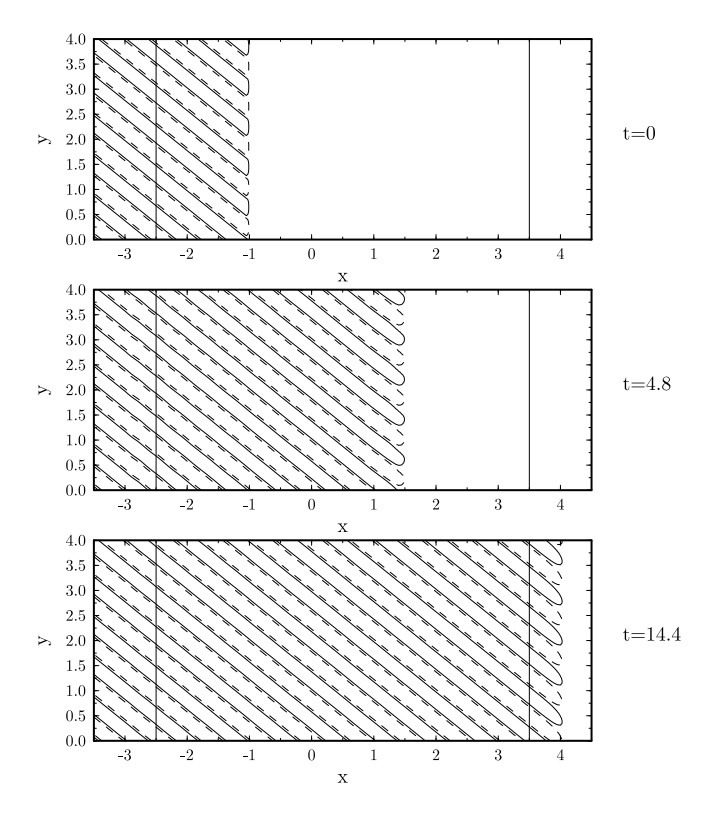


Figure 25. Instantaneous velocity contours at indicated moments, simulating a plane vorticity wave convecting with the mean flow.

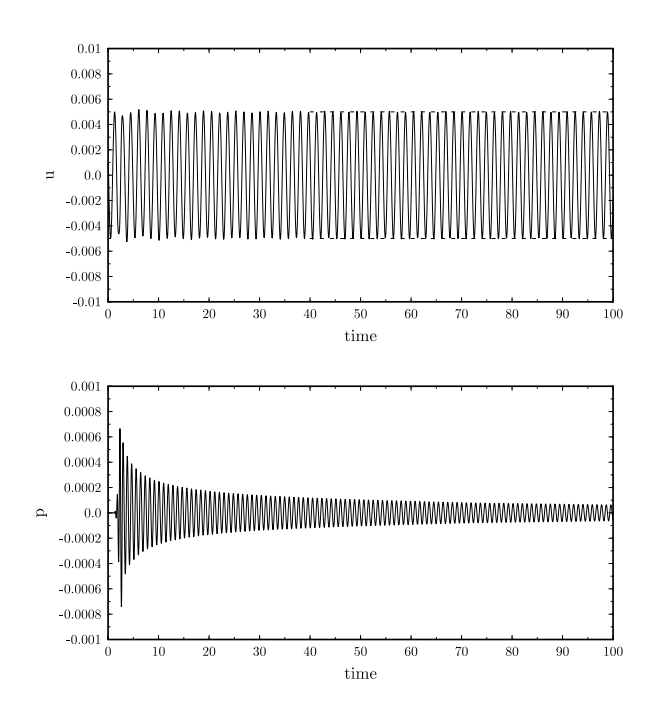


Figure 26. Velocity and pressure history at (x, y) = (-2, 0).

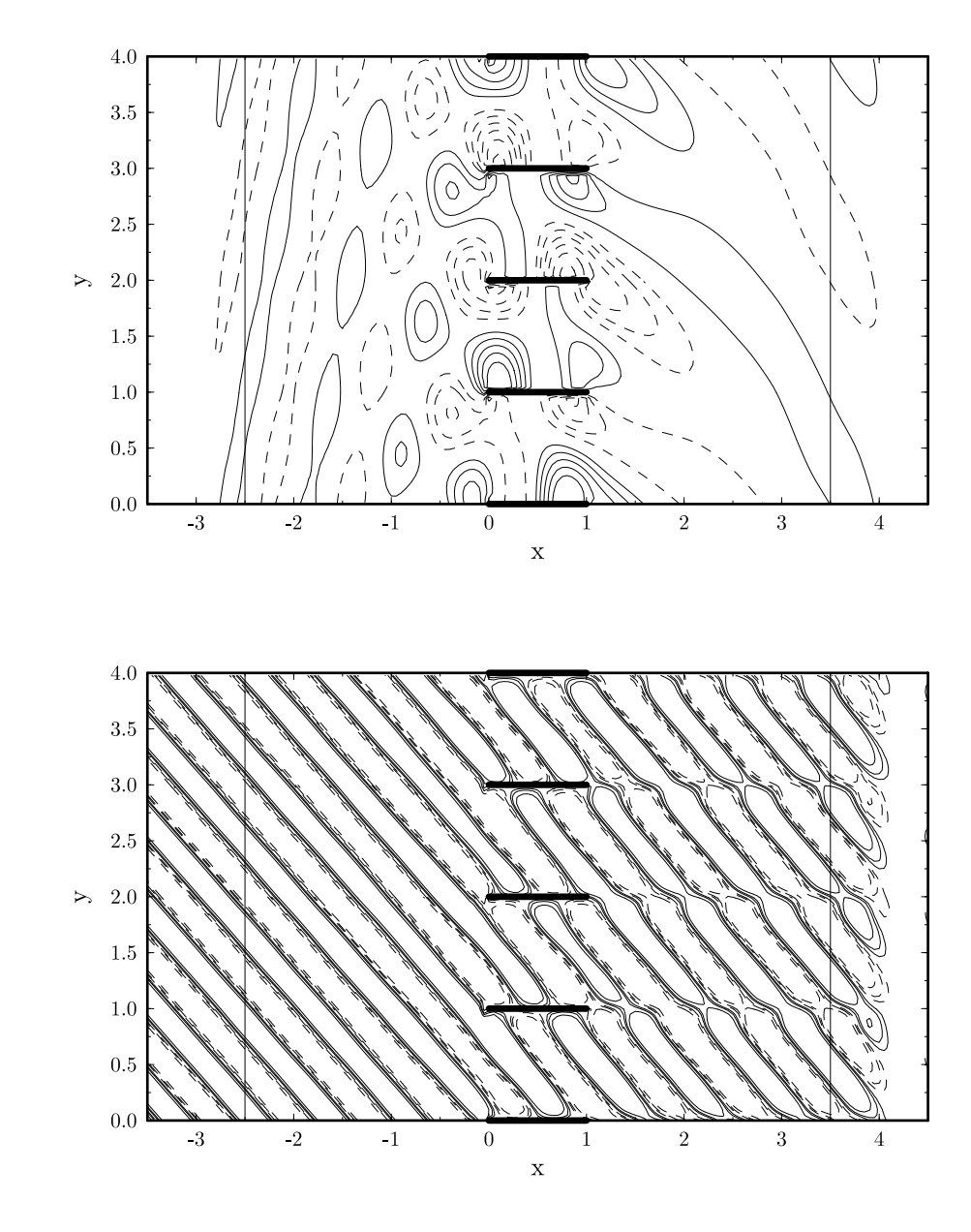


Figure 27. Instantaneous v-velocity and pressure contours. Probelm 2, low frequency case.

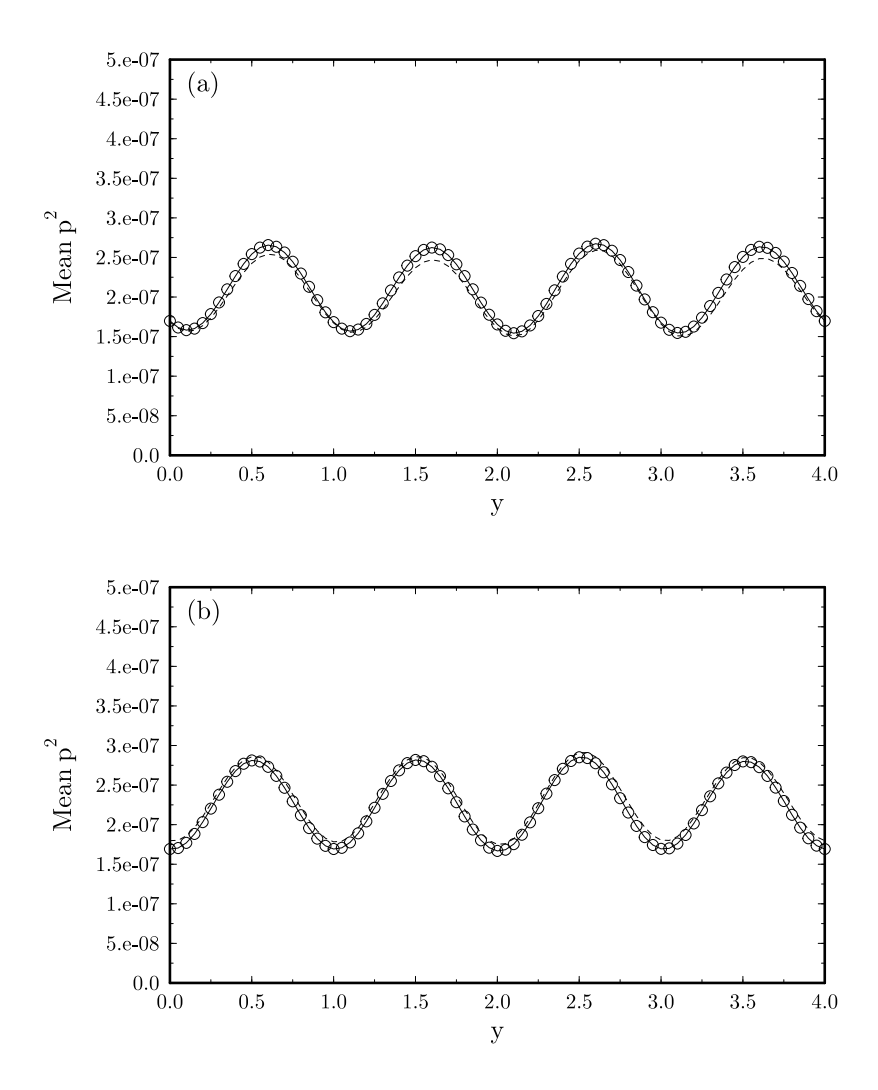


Figure 28. Sound intensity. Low frequency case. (a) x = -2, (b) x = 3. - - - Problem 1, —, Problem 2, o Problem 3.

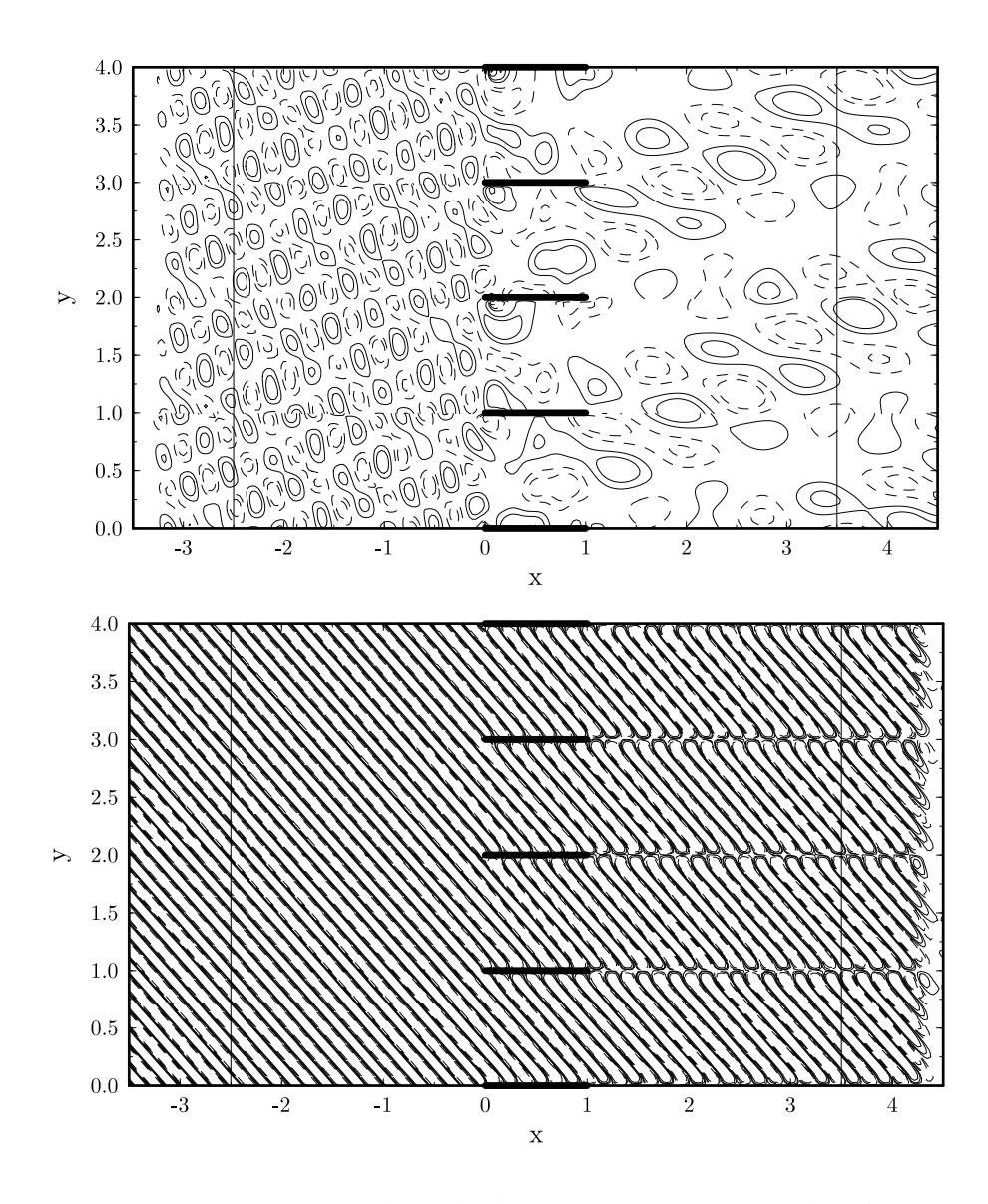


Figure 29. Instantaneous pressure (top) and v-velocity (bottom) contours. High frequency case.

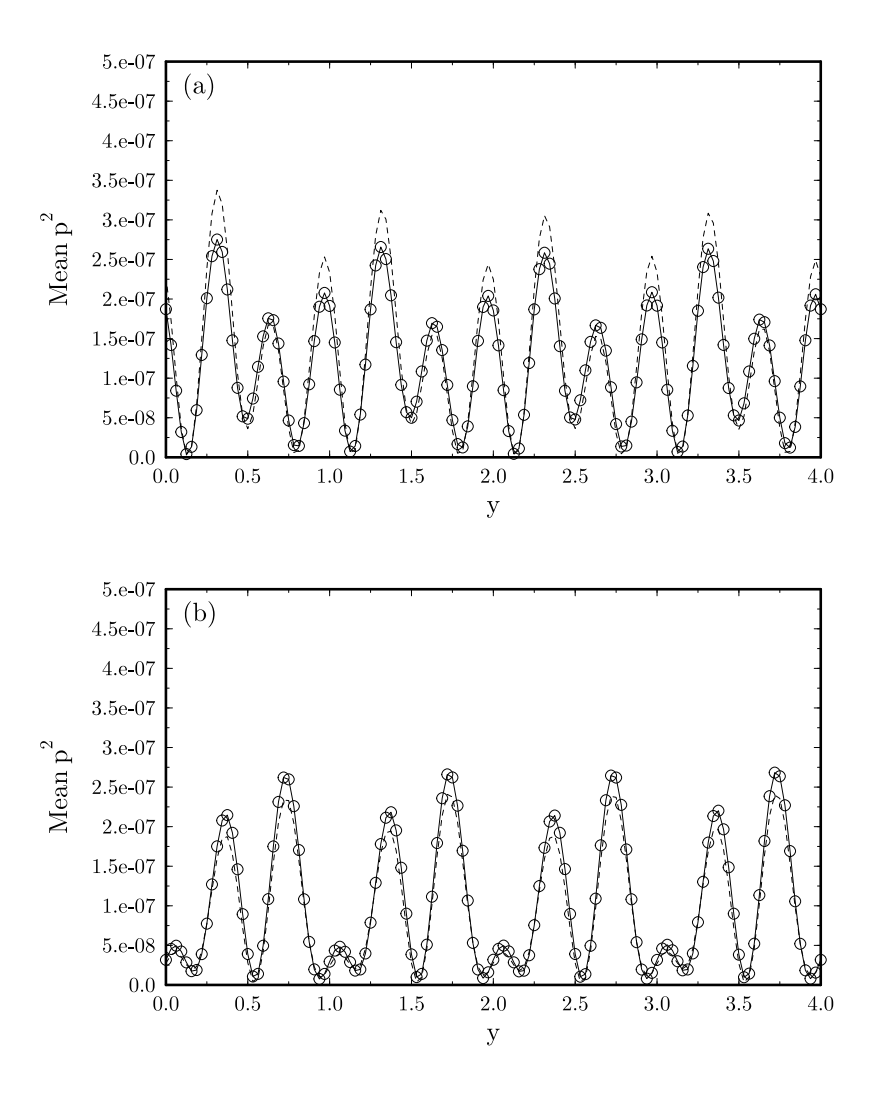


Figure 30. Sound intensity. High frequency case. (a) x = -2, (b) x = 3. - - - Problem 1, ———, Problem 2, o Problem 3.